Simulation of Solid-liquid Mixture Solidification in a Seven-Pin Channel

by

Md. Abdul Malek SONER*, Yu HASEGAWA*, Tatsuya MATSUMOTO**,
Koji MORITA*** and Werner MASCHEK†

Abstract

Analysis of penetration and solidification of hot core-materials mixture into a colder flow channel during core disruptive accidents (CDAs) is one of the major concerns for the safety design of liquid-metal cooled reactors (LMRs). In order to model the freezing behavior of melt of the postulated disrupted core in a CDA of an LMR and provide data for the verification of a fast reactor safety analysis code (SIMMER-III), a series of basic experiments was performed for the freezing behavior of melt during penetrating into a flow channel. In the experiments, a low-melting-point metal alloy (viz., Wood's metal) and solid metal particles mixtures were used as a stimulant melt, while a stainless-steel seven-pin bundle was used as a flow channel. The melt penetration length and the proportion of frozen mass distribution into the flow channel were measured. The comparison between SIMMER-III simulation and its corresponding experiment indicates that the SIMMER-III code can reasonably represents the melt penetration, relocation and freezing behavior as observed in the experiments. The validation of several key models of SIMMER-III was also discussed for treating melt penetration and freezing behaviors of the solid-liquid multi-phase flows.

1.   Introduction

The freezing and penetration of hot core materials mixture into flow channels are important fundamental thermal-hydraulics phenomena to safety assessment of postulated core disruptive accidents (CDAs) in liquid-metal cooled reactors (LMRs). Initial CDAs may occur due to either transient under cooling or transient overpower conditions without scram the reactor. During the course of such accidents, there is a possibility of the whole core melt down due to overheating the

---

*   Graduate Student, Department of Applied Quantum Physics and Nuclear Engineering
**   Assistant Professor, Department of Applied Quantum Physics and Nuclear Engineering
***   Associate Professor, Department of Applied Quantum Physics and Nuclear Engineering
†   Karlsruhe Institute of Technology, Institute for Nuclear and Energy Technologies, Germany

sub-assembly. In the molten core pools, complex multi-phase flows will be formed due to melting and boiling of core materials, such as fuel fragments, molten fuel, molten steel, fission gas, coolant vapor, refrozen fuel, etc. [1]. The composition of molten core materials and movement of these masses have tremendous feedback on the further course of the accident [2]. **Figure 1** shows a schematic view of this kind of disruptive core of the LMR. The potential for recriticality is mitigated if molten fuel can be rapidly relocated away from the reactor core region through some flow paths. Relocation of molten fuel is strongly influenced by blockage formation and the deposition of a fuel crust over structure [3].

In the transition phase of a CDA, distribution and relocation of disrupted-core material have been one of the key study areas. In particular, freezing of molten fuel on the core structure is a key phenomenon because the dynamics of freezing plays an important role in determining the fuel

Fig. 1 Schematic view of core disruptive accidents of an LMR.

removal from the core region. Therefore, it is quite important to reasonably evaluate the mass distribution of molten fuel and freezing behavior inside the escape flow path around the reactor core region. This is only achieved by using a comprehensive computational tool that systematically models multi-phase thermo-hydraulic phenomena coupled with space-dependent neutronics [4]. In this area, the development of a new code, SIMMER-III, has been conducted at the Japan Atomic Energy Agency (JAEA) in collaboration with the Karlsruhe Institute of Technology (KIT) of Germany and the Commissariat à l'Energie Atomique (CEA), which also includes the Institute de Radioprotection et de Sûreté Nucléaire (IRSN) of France [5]. Since SIMMER-III is expected to become a standard tool for fast reactor safety analysis with likely application to licensing calculations, including consequence evaluation in probabilistic safety assessment, the code must be demonstrated to be sufficiently robust and reliable.

Our previous studies focused on basic physical characteristics associated with penetration and freezing behavior of pure molten metal (pure melt) [6,7]. However, understanding of the solid-liquid multi-phase freezing behavior of the transition phase in CDAs is still limited partly owing to difficulties in conducting related experiments to describe the accidents. In this context, a series of basic experiments was performed to simulate the melt penetration and freezing behavior into seven-pin channel using molten-metal/solid particles (particle-mixed melt) and to provide data for the verification of the code [8]. Numerical simulations on these experiments using the SIMMER-III code were also performed and the SIMMER-III simulation results were compared with experimental results as basic code verification. Although in the SIMMER-III code there are some models that take into consideration the extra influence of solid particles on the behavior of multi-phase flows, such as particle viscosity model and the particle jamming model, so far little work has been performed toward the verification of the validity of the SIMMER-III code on simulating this kind of behavior. Therefore, the effectiveness of particle viscosity model and particle jamming model of SIMMER-III was also discussed for the multi-phase melt penetration and freezing behavior.
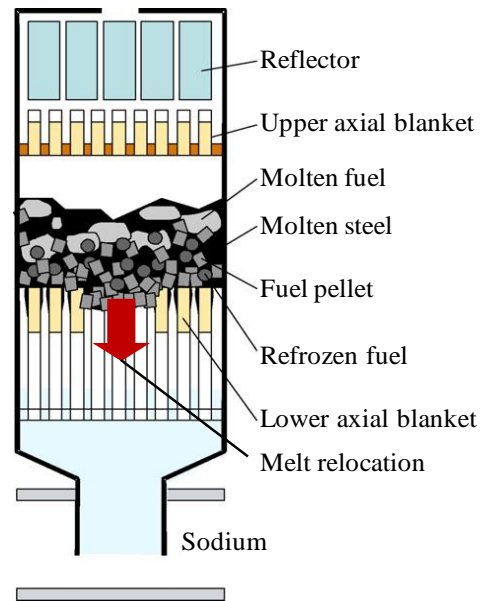
2. Experiments

2.1 Experimental set-up

Figure 2 shows a schematic view of the experimental apparatus. This apparatus consists of a melt tank and flow channel. The melt tank is made of Pyrex glass with a plug made of Teflon. The lengths of the neck of the melt tank and the channel section are 80 mm and 500 mm, respectively. A total of 21 k-type thermocouples are connected to the pin and melt tank to measure temperatures along the pins and flowing melt. The pins are stainless steel (SS) tubes, each closed off at the top, and encased by an outer circular wall made of Pyrex glass to allow for visual observations. The entire set-up is placed on an SS base and supported by a fixed stand. A digital video camera is used to record the melt flow and freezing behavior during the interaction of pin structure.
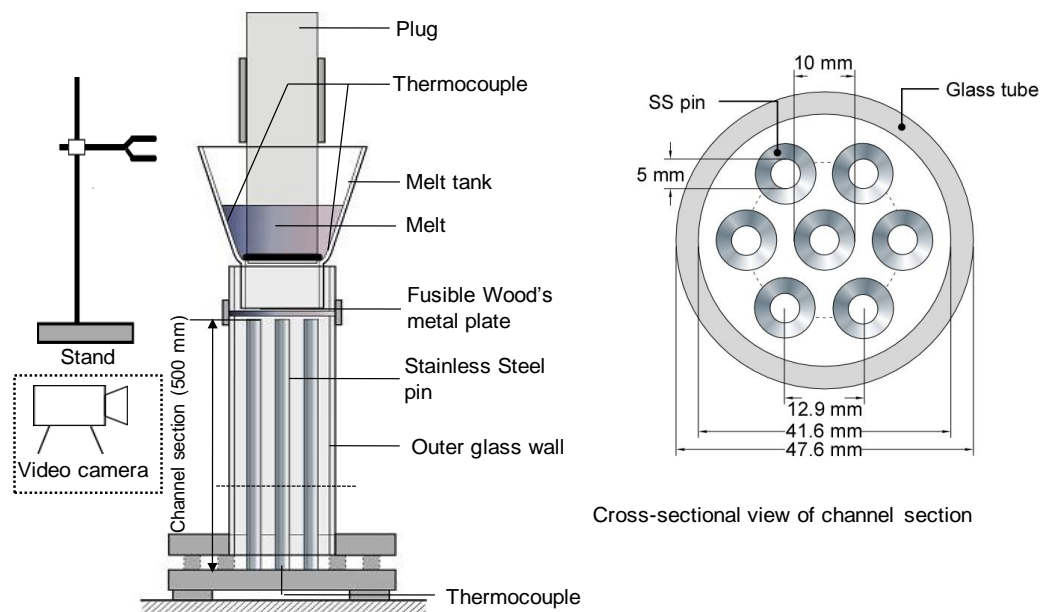

Fig. 2 Schematic diagram of seven-pin bundle experimental apparatus.

The hydraulic parameters used in the seven-pin bundle experiments are summarized in **Table 1**. The hydraulic diameter of the channel, excluding the outer air gap that is present in our series of experiments, is rather larger than that of typical nuclear reactor conditions. This developed out of a need to find a convenient means to observe the melt flow and freezing behavior.

Table 1 Hydraulic parameters for the seven-pin channel experiments.

Parameter	Value
Number of fuel pins	7
Outer pin diameter (mm)	10
Inner pin diameter (mm)	5
Pin pitch (mm)	12.9
Hydraulic diameter excluding outer gap (mm)	8.31
Inner diameter of the outer glass wall (mm)	41.6
Outer diameter of the outer glass wall (mm)	47.6
Thickness of the outer glass wall (mm)	3

2.2 Experimental procedure and conditions

A thin fusible (~0.5 mm thickness) solid plate of Wood's metal was initially set at the base of the melt tank is to ensure smooth injection of melt into the channel. The pins of the flow channel structure were uniformly heated by blowing hot air from the top to the bottom of the channel. The temperature of the pins was monitored using a computerized thermocouple device. At the same time, a weighed amount of solid Wood's metal and spherical solid bronze particles (0.5 mm diameter) was heated by an electric heater; the temperature of the melt was monitored using a digital thermometer and transferred to the melt tank. After obtaining the desired temperatures for both the pins and melt, and mixing the melt homogenously, the plug was pulled up to allow the melt to drain through to the channeling structure. The melt flows and freezing behavior into the channels were recorded using a digital video camera. The adhered frozen material to pin surfaces and other fragments were collected after each experiment. Local penetration lengths at all six sub-channel positions were measured, with the average of these values then taken as the penetration length. All experiments were conducted at atmospheric pressure. **Table 2** lists some physical properties of Wood's metal and SS. The initial conditions of experiments are summarized in **Table 3**.

Table 2 Physical properties of Wood's metal [6,9] and stainless steel [10,11].

Parameters	Wood's metal	Stainless steel (Type 316)
Melting point (°C)	78.8	1430
Boiling point (°C)	1760	2600
Density (kg/m^3)	8400	8000
Thermal conductivity (W/m·K)	11.1	16.2
Specific heat (J/kg·K)	150	530
Kinematic viscosity (m^2/s)	2×10^{-7}	1.97×10^{-7}
Latent heat of fusion (J/kg)	2.53×10^4	3.39×10^5
Surface tension (N/m)	1.0	1.13
Composition	Bi, Sn, In	Fe, Cr, Ni, Mo

Table 3 Experimental conditions.

Pin temp. (°C)	Melt mass (g)	Melt temp. (°C)	Particle volume fraction (%)
25	175	90 -130	0 and 20
25	175	100	0 – 30
25 - 50	175	100	0 and 20

3. Numerical Simulation

3.1 Phase-change model of SIMMER-III

SIMMER-III is a two-dimensional, multi-velocity-field, multi-phase, multi-component, Eulerian, fluid-dynamics code coupled with a fuel-pin model and a space- and energy- dependent neutron kinetics model [5]. The fundamental equations of the fluid dynamics are based on a so-called multi-fluid model. Heat transfer between melt and structures results in the melting of structures and/or freezing of melt. SIMMER-III describes the melting/freezing process in two steps. The first step calculates the phase-change process occurring at interface between melt and structures, which are described by a non-equilibrium heat transfer-limited model. The non-equilibrium process means that the bulk temperature generally does not satisfy the phase-change condition when the

mass transfer occurs at the interface. The second step describes the mass and energy transfer is through an equilibrium process when bulk temperatures satisfy the phase-change condition.

The non-equilibrium melting/freezing transfers can include particle formation in the melt flow that contributes to equilibrium (bulk) freezing. The basic concept of non-equilibrium mass transfer model is described in **Fig. 3**, where a binary contact interface of the energy components A and B is shown. This is a heat transfer-limited process where the phase-change rate is determined from an energy balance at the interface [12]. Energy transfers between components are based on the interfacial area and heat-transfer coefficients. A specified temperature is assigned to each possible interface to calculate heat flows from/to each interface into/from the respective bulk materials. These heat flows are summed to give the net interfacial energy loss or gain. The net energy transfer rate from the interface is defined as

$$q^I_{A,B} = a_{A,B} \left\{ h_{A,B} \left(T^I_{A,B} - T_A \right) + h_{B,A} \left(T^I_{A,B} - T_B \right) \right\}, \tag{1}$$

Where a is the interfacial area per unit volume, h is the heat transfer coefficient, T is the temperature and the superscript I refers to the interface.
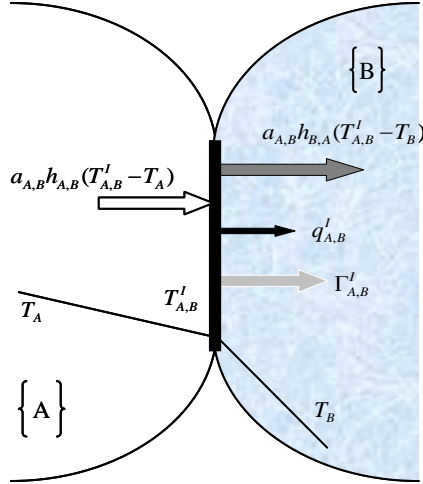

Fig. 3 Basis of non-equilibrium heat and mass transfer limited process.

An interfacial energy loss is defined as being positive and means freezing must occur to conserve (provide) energy. An interfacial energy gain is defined as being negative and means energy is going into melting. For example, **Fig. 3** shows the A–B interface where the interface is undergoing a net loss of energy to component B. This energy is coming from the freezing of component A. The resulting product will be either more of component B or another component depending on the process involved.

The phase-change rate is determined from the energy balance at the interface. If the net heat flow $q^I_{A,B}$ is zero, sensible heat is exchanged without phase change at the interface. If $q^I_{A,B}$ is positive, namely the energy is lost at the interface, the molten material freezes. The mass-transfer rate for this case is

$$\Gamma^I_{A,B} = \frac{q^I_{A,B}}{i_A - i_{sol}}, \tag{2}$$

where i is the enthalpy and the subscript *sol* refers to the solidus point. If $q_{A,B}^{I}$ is negative, namely, the energy is gained at the interface, the structure component melts and the mass transfer rate is

$$\Gamma_{B,A}^{I} = -\frac{q_{A,B}^{I}}{i_{liq} - i_{B}},$$

(3)

where the subscript *liq* refers to the liquidus point.

When a phase change is predicted, the interface temperature $T_{A,B}^{I}$ is expressed as a phase-change temperature such as the liquidus or solidus temperature. Thus the equivalent interface/phase-change temperature when there is no mass-transfer, with $q_{A,B}^{I}$ being zero, is

$$T_{A,B}^{I} = \frac{h_{A,B}T_A + h_{B,A}T_B}{h_{A,B} + h_{B,A}}.$$

(4)

The equilibrium melting/freezing transfer rate is determined when the bulk temperatures of structure or particles exceed the solidus temperature or when liquid bulk temperatures drop below the liquidus temperature. If the internal energy of liquid component B drops below its liquidus energy $(e_B < e_{liq})$, component B freezes as component A, and the corresponding mass-transfer rate is

$$\Gamma_{B,A}^{EQ} = \frac{1}{\Delta t}\frac{e_{liq} - e_B}{h_f}\bar{\rho}_B,$$

(5)

where Δt is the time-step size, the superscript *EQ* refers to the equilibrium process, $\bar{\rho}$ is the macroscopic density and h_f is the heat of fusion. If the internal energy of solid component A exceeds its solidus energy $(e_A > e_{sol})$ then component A melts into component B and the corresponding mass-transfer rate is

$$\Gamma_{A,B}^{EQ} = \frac{1}{\Delta t}\frac{e_A - e_{sol}}{h_f}\bar{\rho}_A.$$

(6)

3.2 Particle viscosity model

To simulate the penetration of molten core materials into a colder structure channel and their blockage formation during a CDA, it is important to simulate the effective increase in the fluid viscosity of the materials due to the existence of solid particles in the molten mixture. A particle viscosity model based on Russel's study [13] was introduced to the SIMMER-III code using the following formulation [14]:

$$\mu_C = \mu_L\left\{\frac{\alpha_L}{\alpha_L + \alpha_P} + \frac{f\alpha_{MP}\alpha_P}{\alpha_{MP}(\alpha_L + \alpha_P) - \alpha_P}\right\}$$

(7)

where μ_C is the effective viscosity of the continuous liquid phase, μ_L is the viscosity of the liquid phase, α_P is the particle volume fraction and $\alpha_{MP} = 0.62$ is the maximum volume

fraction of solid particles. Equation (7) is used in the SIMMER-III code with the model parameter $f = 5.0$. This equation realizes the smooth change of effective viscosity over the wide range of particle volume fraction.

The particle viscosity model was originally introduced to SIMMER-III for simulation of the penetration and blockage formation of molten core materials in a flow channel. The blockage formation is simulated by increasing the effective viscosity sharply, owing to the mixing of solid particles with the melt, when the fraction of solid particles in the melt exceeds roughly 60%. In this study, the influence of this particle viscosity model to the momentum exchange function on the melt penetration and freezing behavior in a seven-pin channel will be discussed.

3.3 Particle jamming model

A particle jamming model was also developed in SIMMER-III in order to appropriately simulate the blockage formation of molten core materials when penetrating into a flow channel. In SIMMER-III, this is modeled by inhibiting the inflow of solid particles into a computational mesh cell when the volume fraction of solid particle in the cell exceeds a maximum packing fraction by assigning a large value to the momentum exchange function at the cell interface. The idea behind the particle jamming model is to define a function of the volume fraction of particles, which increase exponentially with the increase of particle volume fraction and become large as the maximum packing fraction is approached in a computational mesh cell. Using the same function used in SIMMER-II [15], a particle jamming function was introduced to the SIMMER-III code. The function is based on the assumption that when the solid particle volume fraction is smaller than a defined maximum packing fraction, then the function remains equal to zero, but when the solid particle volume fraction approaches the maximum packing fraction, then the function will rapidly increase to an infinite value. This particle jamming model is expressed by the following formulation [14]:

$$\phi = \max\left\{1 - \frac{\max(\alpha_P - \alpha_{PJ\max}\beta_{PJ}, 0)}{\alpha_{PJ\max}(1 - \beta_{PJ})}, 0.1\right\}^{C_{PJ}} - 1$$

(8)

where $\alpha_{PJ\max} = 0.7$ is the maximum volume fraction of solid particles while $\beta_{PJ} = 0.95$ is the fraction of $\alpha_{PJ\max}$ above which the particle jamming model is applied. The model parameter C_{PJ} is set to -10.0. This function remains zero (*i.e.* $\phi = 0.0$) if α_P is not larger than $\alpha_{PJ\max}\beta_{PJ}$ and increases rapidly to $0.1^{C_{PJ}} - 1$ (i.e. $\phi = 0.1^{C_{PJ}} - 1$) when α_P exceeds $\alpha_{PJ\max}\beta_{PJ}$. In this study, the effect of this model will be discussed.

3.4 Modeling a seven-pin channel experiment using SIMMER-III

Figure 4 indicates a schematic view of the distribution of mesh nodes and the initial material distributions in terms of volume fractions used in the SIMMER-III calculations for the corresponding experimental setup shown in **Fig. 2**. In the calculations, six regions, the fuel pin, the outer wall, the gas with outer wall, the melt tank, the cover gas, the outer wall exit, were modeled by two-dimensional cylindrical geometry to represent experimental conditions. The mesh scheme introduced for the calculation by SIMMER-III was two nodes in the radial direction and 60 nodes in the axial direction. The first row of radial cells was assigned to the central pin and six

surrounding pins with associated surrounding fluid (air), and the second row to the remaining structures and surrounding fluid. Mesh nodes were 17.9 mm and 5.9 mm in the radial direction for the first and second rows, respectively, and 10 mm in the axial direction. The melt pool was represented at the top of the fuel pin by eight mesh cells in the axial direction and the first row in the radial direction. The molten metal ejected downward under the influence of gravity at atmospheric pressure and passed through the flow channel. The calculation was started after the onset of the melt ejection into the channel. The present analytical model for melt penetration and freezing behavior describes the heat and mass transfers among the molten Wood's metal, the frozen melt, the bronze particles and the structure (pins).
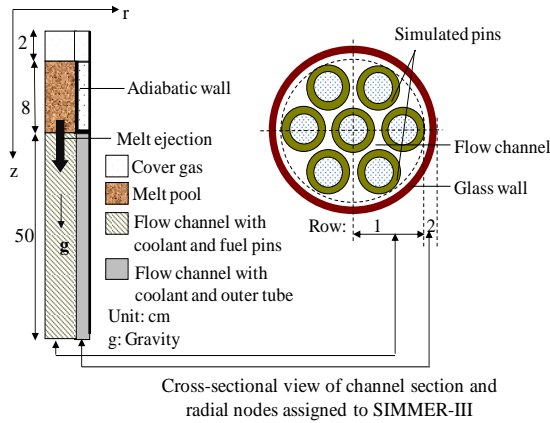

Fig. 4 Mesh nodes for SIMMER-III and initial material distributions in the calculation.
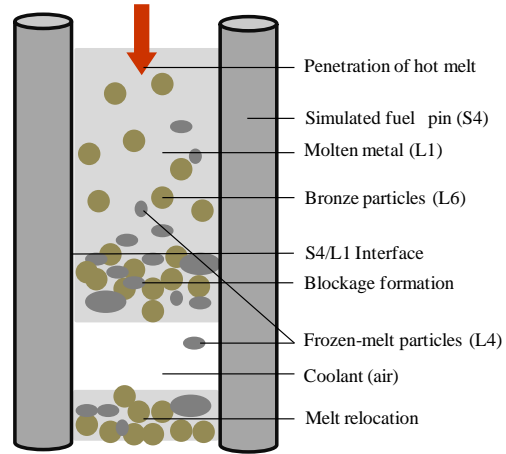

Fig. 5 Modeling concept of the melt penetration behavior between pins.

The concept of the heat and mass transfer model for the present experimental analyses using SIMMER-III is illustrated in **Fig. 5** schematically. In this model for freezing phenomena of melt, four components such as molten metal, frozen-melt particles, bronze particles and pins are assigned to mass and energy components and are expressed as L1, L4, L6 and S4 respectively, according to the indices commonly used in SIMMER-III. Here, molten metal solidified in fluid (air) is treated as frozen-melt particles. The particle-mixed melt interacts with pins, particles and bronze particles at the L1/S4, L1/L4, L6/S4, L1/L6 and L4/L6 interfaces, respectively.

Both non-equilibrium and equilibrium freezing processes of molten metal are considered in this model. In the present analyses, penetration behaviors of molten metal are represented by the freezing mass transfer rates per unit volume, $\Gamma_{L1,L4}^{I(L1/S4)}$, $\Gamma_{L1,L4}^{I(L1/L4)}$ and $\Gamma_{L1,L4}^{EQ}$. Here, the superscripts I(L1/S4) and I(L1/L4) refer to non-equilibrium mass transfers at the L1/S4 and L1/L4 interfaces, respectively. The subscript "L1,L4" refers to particle (L4) formation from molten metal (L1) as shown in **Table 4**. On the other hand, although re-melting of the solidified particles might have only minor effects on the freezing behavior under the present experimental conditions, two melting mass transfer rates are also considered: $\Gamma_{L4,L1}^{I(L1/L4)}$ and $\Gamma_{L4,L1}^{EQ}$.

Table 4 Non-equilibrium mass-transfer paths.

	Interface				
	Melt/Pin (L1/S4)	Melt/Particles (L1/L4)	Bronze particles/Pin (L6/S4)	Melt/Bronze particles (L1/L6)	Particles/Bronze particles (L4/L6)
Freezing	melt→particle	melt→particle	×	×	×
Melting	×	particle→melt	×	×	×

For the present analyses, the intracell heat and mass transfers among the components of molten metal, frozen-melt particles and bronze particles are expressed by the following mass and energy conservation equations without convection terms:

(Molten metal)

$$\frac{\partial \overline{\rho}_{L1}}{\partial t} = [\Gamma_{L4,L1}^{I(L1/L4)} - \Gamma_{L1,L4}^{I(L1/L4)} - \Gamma_{L1,L4}^{I(L1/S4)}] + (\Gamma_{L4,L1}^{EQ} - \Gamma_{L1,L4}^{EQ}), \qquad (9)$$

$$\frac{\partial \overline{\rho}_{L1} e_{L1}}{\partial t} = \Gamma_{L4,L1}^{I(L1/L4)} e_{liq} - [\Gamma_{L1,L4}^{I(L1/L4)} + \Gamma_{L1,L4}^{I(L1/S4)}] e_{L1} + (\Gamma_{L4,L1}^{EQ} e_{sol} - \Gamma_{L1,L4}^{EQ} e_{liq})$$

$$+ a_{L1,L4} h_{L1,L4} (T_{L1,L4}^{I} - T_{L1}) + a_{L1,L6} h_{L1,L6} (T_{L1,L6}^{I} - T_{L1})$$

$$+ a_{L1,S4} h_{L1,S4} (T_{L1,S4}^{I} - T_{L1}), \qquad (10)$$

(Frozen-melt particles)

$$\frac{\partial \overline{\rho}_{L4}}{\partial t} = [\Gamma_{L1,L4}^{I(L1/L4)} - \Gamma_{L4,L1}^{I(L1/L4)} + \Gamma_{L1,L4}^{I(L1/S4)}] + (\Gamma_{L1,L4}^{EQ} - \Gamma_{L4,L1}^{EQ}), \qquad (11)$$

$$\frac{\partial \overline{\rho}_{L4} e_{L4}}{\partial t} = [\Gamma_{L1,L4}^{I(L1/L4)} + \Gamma_{L1,L4}^{I(L1/S4)}] e_{Sol} - \Gamma_{L4,L1}^{I(L1/L4)} e_{L4} + (\Gamma_{L1,L4}^{EQ} e_{Sol} - \Gamma_{L4,L1}^{EQ} e_{Liq})$$

$$+ a_{L1,L4} h_{L1,L4} (T_{L1,L4}^{I} - T_{L4}) + a_{L6,L4} h_{L6,L4} (T_{L6,L4}^{I} - T_{L4})$$

$$+ a_{S4,L4} h_{S4,L4} (T_{S4,L4}^{I} - T_{L4}) \qquad (12)$$

(Bronze particles)

$$\frac{\partial \overline{\rho}_{L6} e_{L6}}{\partial t} = a_{L1,L6} h_{L1,L6} (T_{L1,L6}^{I} - T_{L6}) + a_{L4,L6} h_{L4,L6} (T_{L4,L6}^{I} - T_{L6})$$

$$+ a_{S4,L6} h_{S4,L6} (T_{S4,L6}^{I} - T_{L6}) \qquad (13)$$

Here, $\overline{\rho}$ is the macroscopic density defined as the product $\alpha\rho$ of the volume faction α and microscopic density ρ, e is the specific internal energy, a is the binary contact area per unit volume, h is the heat transfer coefficient and T^{I} is the interface temperature.

For the pins, the following energy equations with only heat-transfer terms are solved for the intracell heat transfer.

(Pins)

$$\frac{\partial \overline{\rho}_{S4} e_{S4}}{\partial t} = a_{L1,S4} h_{L1,S4} (T^I_{S4,L1} - T_{S4}) + a_{L4,S4} h_{L4,S4} (T^I_{S4,L4} - T_{S4})$$

$$+ a_{L6,S4} h_{L6,S4} (T^I_{S4,L6} - T_{S4}) \qquad (14)$$

4. Results and Discussion

In the present experimental simulations using SIMMER-III, the effect of the particle viscosity model and the particle jamming model was examined, to observe the effects of particles on penetration and freezing characteristics of melt flow into the seven-pin channel. To better understand the transient freezing behavior, the time dependency of melt penetration into the channel was also measured. There was no evidence that wetting of the SS metal structure by molten metal had occurred [7,16]. This paper will mainly present comparisons between the experimental and SIMMER-III simulated results of the melt penetration, relocation and freezing behavior. In addition, simulation results both with and without the application of the momentum exchange function term coupled with the particle viscosity model are presented in this paper together with the corresponding experimental results. In all of the following figures, MXF ON/OFF refers to simulations by the SIMMER-III code; the particle viscosity model is applied (ON) and not applied (OFF) to the momentum exchange function.

4.1 Effect of melt temperature

The experiments were conducted by varying the melt temperatures within the range of 90–130°C. The volume fraction of bronze particles in the mixture is 20 %. The penetration length of melt is defined as the average of the maximum length of solidified melts from all sub-channels (six in our experiments). **Figure 6** shows the penetration lengths of melt as a function of melt temperatures. It can be seen from the figure that penetration length increased with increasing melt temperature. For higher melt temperatures, more time was necessary for the melt to cool to its freezing point; hence, the melt retained fluidity for longer and penetrated farther. The penetration length of different experimental cases is compared with their corresponding SIMMER-III simulation results. Comparison between the simulated and experimental results show that the SIMMER-III simulation with the particle viscosity model is applied to the momentum exchange function gives overestimation of the penetration length. On the other hand, the simulation results without the particle viscosity model agree quite well with their corresponding experiments. The penetration length here is defined as the distance that the particle-mixed melt flowed in the first row of radial cells. Since almost uniform penetration of the melt was observed around the seven pins in radial and circumferential directions in the experiments, the penetration length can be compared consistently between experiments and simulations with the present mesh nodes (*i.e.,* one node for pin structures).
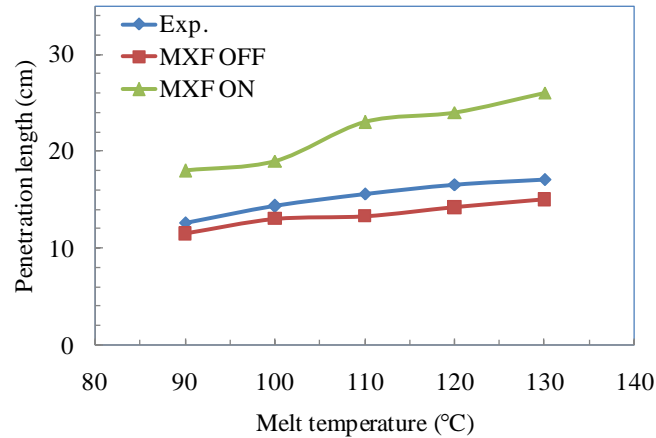
Fig. 6 Average penetration length of melt at different melt temperatures (melt mass: 175 g, pin temp.: 25°C).

4.2 Effect of particle volume fraction

4.2.1 Experimental observation

Experiments were conducted wherein volume fraction of bronze particles in melt was varied in the range 0–30%. **Figure 7** shows photographs of frozen melt on pin surfaces at different volume fractions of particles. We observed in the experiment involving higher volume fraction (>10 vol.%) that crust formed over the upstream portion while particle aggregations formed in the downstream portion of the melt adhesion. While solid particles in mixed melts are co-moving with pure melt inside the pin channel, velocities at the leading edge of the melt can fall for short times to nearly zero, and particle aggregates can form that temporarily hinder melt flows. Jamming of particle aggregates at different locations was found at the leading edge of the particle-mixed flow. We found furthermore that some particle-mixed melt with higher particle concentrations separated from the main flow and flowed to the structure bottom. Separated melt mass increases with increasing particle volume fraction due to melt separation behavior. As a result, we found shorter final penetration lengths of particle-mixed melt than those in the pure melt (0 vol.% of particles) cases.
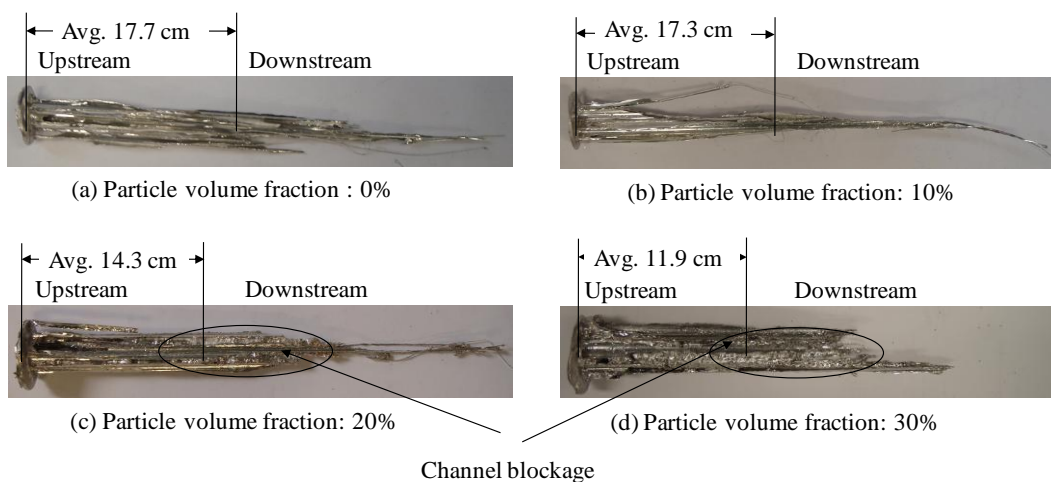

(a) Particle volume fraction : 0%

(b) Particle volume fraction: 10%

(c) Particle volume fraction: 20%

(d) Particle volume fraction: 30%

Channel blockage

Fig. 7 Photographs of frozen melt on pin surfaces at different volume fractions of particles (melt mass: 175 g, pin temp.: 25°C, melt temp.: 100°C).

4.2.2 Quantitative measurement

In previous studies, particle effects on flowing-melt solidification have not been well investigated. The effective viscosity of the mixture could increase as solid particle volume fraction increase in the melt. At small volume fractions, these particles have a negligible effect on melt viscosity. As volume fraction increases in the melt, viscosity rises very rapidly [10,17]. Given these circumstances, the particles become more closely packed together and high mobility with melt would be more difficult to attain. Particle-particle interactions then come into effective, and the effective viscosity of mixed melts increases. **Figure 8** shows melt penetration length at different solid particles volume fraction. It can be seen from the figure that penetration lengths decreasing with increasing solid particle volume in melt. The higher volume fraction of bronze particles might also enhance the effective thermal conductivity of the mixed melt. Due to experimental limitations, we were unable to perform measurements on melts with volume fractions greater than 30 vol.% of solid particles. Comparison between the simulated and experimental results show that the SIMMER-III with the particle viscosity model reasonably represents the penetration length for pure melt, whereas it overestimates the penetration length for particle-mixed melt with the corresponding experimental results. It can also be seen from the figure that the results simulated by the SIMMER-III code without the particle viscosity model successfully produces trends of penetration length similar to those observed in experiments for pure and particle-mixed melts. This is because in the simulations without the particle viscosity model some melt is separated from the main flow stream and flows to the structure bottom. As a result, penetration length becomes shorter.
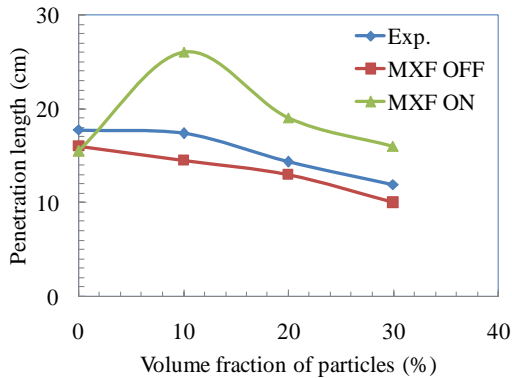

Fig. 8 Penetration length at different volume fraction of bronze particles (melt mass: 175 g, melt temp.:100°C, pin temp.: 25°C).
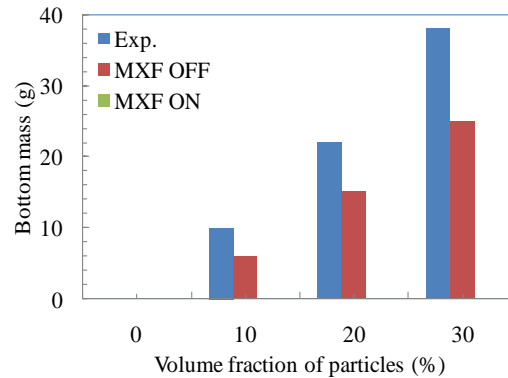
Fig. 9 Collected bottom mass at different volume fraction of particles (melt mass: 175 g, melt temp.: 100°C, pin temp.: 25°C).

Figure 9 is a mass histogram showing that the collected melt mass increases with increasing volume fraction of solid particles. From experiments and SIMMER-III simulations, it is most interesting to note that for pure melt all of the melt injected froze into the pin channel, while for particle-mixed melt, melt separation was observed. For particle-mixed melt, comparisons of separated mass show reasonable agreement between the experimental and SIMMER-III simulation results without the particle viscosity model. In contrast, no melt separation was observed when particle viscosity model is applied. The melt separation was mainly due to fact that the pure melt can readily solidify onto pin surfaces but particles cannot. Therefore, as pure melt solidifies out and particles continue to fall, particle concentrations increase in downstream portions of the melt. In addition, certain factors might also be important for melt separation such as structural geometry, different thermal conductivity and density between particles and molten metal, and particle–particle interactions. We further found higher particle concentrations in the collected melt than in melt adhesions. It seems that SIMMER-III can reasonably well represent the effect of solid particles on

melt relocation and distribution into the flow channel. On the other hand, the particle jamming model did not show any obvious influence on the results under the present experimental conditions. This may be due to the low concentration of the solid particles used in this study.

4.3 Effect of pin temperature

Experiments were conducted by varying the pin temperature in the range 25–50°C. **Figure 10** shows the penetration lengths of particle-mixed melts as a function of pin temperature. It is clearly seen from the figure that the penetration length increased with increasing pin temperature. This is because heat transfer is reduced at higher pin temperature, which tends to slow cooling of the melt, and hence it lengthens melt penetration. It can be seen from the figure, the penetration length can be compared consistently between experiments and SIMMER-III simulations without the particle viscosity model. It can also be seen from the figure that the results simulated by the SIMMER-III code with the particle viscosity model overestimate penetration length compared with their corresponding experiments.
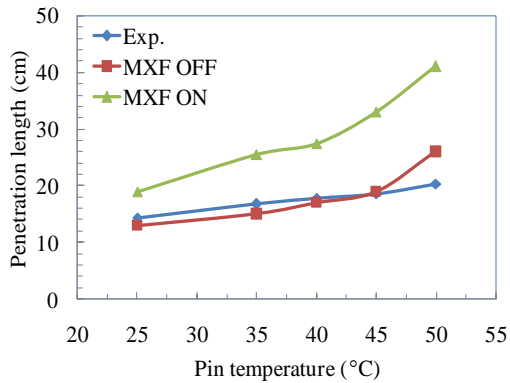

Fig. 10 Average penetration length of melt at different pin temperatures (melt mass: 175 g, melt temp.: 100°C).
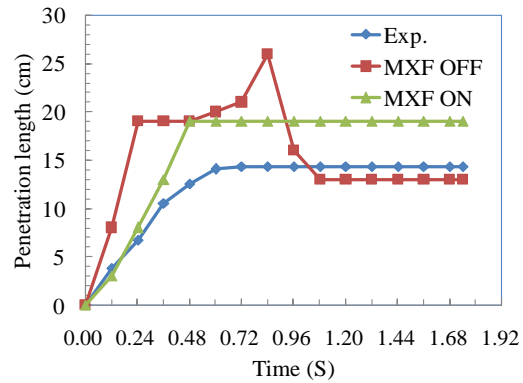
Fig. 11 Transient penetration length of melts into the channel (melt mass: 175 g, pin temp.: 25°C, melt temp.: 100°C).

The transient penetration lengths of the experiments and the SIMMER-III simulations are presented in **Fig. 11**. In the experiments, the transient melt positions were determined from images recorded with a digital video camera. The simulation results shown in the figure indicate that the final penetration length reasonably agrees with the experimental result when the particle viscosity model is not applied. It is noted that at the early stage of the simulation the melt penetration length includes the leading part of the melt as well as the following main flow stream. At the later stage some melt of the leading part separates from the main flow stream without adhesions to the pin surface and finally falls at the structure bottom. Therefore, at the early stage in the two simulations the melt penetrates the flow channel longer within a short time in comparison with the experimental results. In the simulation without the particle viscosity model, after that the melt penetration length decreases rapidly due to the melt separation. However, in the experiment the transient penetration length shown in **Fig. 11** was determined only by the main flow stream without the leading part of the melt due to measurement limitation. It can be also seen from the figure that SIMMER-III simulations with the particle viscosity model overestimates the transient penetration into the channel compared with the experimental results.

5. Conclusion

In this study, a series of experiments has been performed to simulate the behavior of the penetration and freezing in presence of solid particles in melt into a seven-pin channel in order to verify the applicability of the fast reactor safety analysis code, SIMMER-III. In the present experiments, the penetration length was seen to increase with increasing melt and pin temperatures. The penetration length decreased with increasing solid particle volume fraction of mixed melts. It is to be mentioned here that for higher volume fraction of particles in melt, the channel was blocked due to particle jamming.

It was found that in experiments and SIMMER-III simulations for pure melt one freezing mode among all melt adhered to the pin surface, whereas in particle-mixed melts a separation of melt occurred, and hence we observed two freezing modes in melt adhesions in addition to a small amount of separated melt at the pins bottom. Comparisons between the results of the SIMMER-III simulations and its corresponding experiments demonstrate that SIMMER-III without the particle viscosity model can reasonably represent the penetration length, distribution and freezing behavior of pure melt and particle-mixed melt flows. In addition, the particle jamming model shows no obvious influence on the obtained penetration length and freezing behavior under the present experimental conditions. We anticipate that the present analysis will contribute to improvements in the reliability of accident analyses of LMRs.

Nomenclature

a	Binary-contact area per unit volume (m^{-1})
$a_{A,B}$	Binary contact area of the A/B interface per unit volume (m^{-1})
e	Specific internal energy ($J\ kg^{-1}$)
g	Gravitational acceleration ($m\ s^{-2}$)
$h_{A,B}$	Heat transfer coefficient for side A of the A/B interface ($Wm^{-2}K^{-1}$)
h_f	Latent heat of fusion ($J\ kg^{-1}$)
i	Specific enthalpy ($J\ kg^{-1}$)
$q^I_{A,B}$	Net heat transfer rate per unit volume at the A/B interface ($W\ m^{-3}$)
T	Temperature (K)
$T^I_{A,B}$	Interface temperature at the A/B interface (K)

Greek Letters

α	Volume fraction
α_S	Volume fraction of structure field
α_P	Volume fraction of solid particles
Δt	Time-step size
$\Gamma^{EQ}_{A,B}$	Equilibrium mass transfer rate per unit volume from component A to B ($kg\ s^{-1}\ m^{-3}$)
$\Gamma^I_{A,B}$	Non-equilibrium mass transfer rate per unit volume from component A to B ($kg\ s^{-1}\ m^{-3}$)
ρ	Microscopic density ($kg\ m^{-3}$)

$\bar{\rho}$ Macroscopic density (kg m^{-3}), $\bar{\rho} = \alpha\rho$

μ_L Viscosity of liquid phase (Pa s)

μ_C Effective viscosity of continuous liquid phase (Pa s)

Subscripts
A, B   Energy component
L1   Liquid metal
L4   Frozen-melt particles
L6   Bronze particles
liq   Liquidus point
sol   Solidus point
S4   Pin

Superscripts
EQ   Equilibrium mass transfer
I   Interface
I(A/B)   Interface identification of the A/B binary contact

References

1) T. G. Theofanous, and C.R. Bell, An Assessment of Clinch River Breeder Reactor Core Disruptive Accident Energetic, Nuclear Science and Engineering, 93, pp. 215-228 (1986).
2) P. Menzenhauer, W. Peppler, et al.; Material Movement, Relocation and Inter-Subassembly Propagation in Bundles Under Simulated Accident Conditions (out-of-pile experiments with thermite), Science and Technology of Fast Reactor Safety, BNES, London, pp. 373-379 (1986).
3) B. W. Spencer, R. E. Henry, et al.; Summary and Evaluation of Reactor-Material Fuel Freezing Tests, Proceedings of the International Meeting on Fast Reactor Safety Technology, Seattle, Washington, August 19-23, pp.1766-1775 (1979).
4) K. Morita, T. Matsumoto, et al.; Experimental Verification of the Fast Reactor Safety Analysis Code SIMMER-III for Transient Bubble Behavior with Condensation, Nuclear Engineering and Design 238(1), pp. 49-56 (2008).
5) Y. Tobita, S. Kondo, et al.; The Development of SIMMER-III, an Advanced Computer Program for LMFR Safety Analysis. Int. Proc. Joint IAEA/NEA Technical Meeting on the Use of Computational Fluid Dynamics Codes for Safety Analysis of Reactor Systems (including Containment), Pisa, Italy, November 11-13 (2002).
6) M. M. Rahman, Y. Ege, et al.; Simulation of Molten Metal Freezing Behavior onto a Structure", Nuclear Engineering and Design, 238, pp. 2706-2717 (2008).

7) M. K. Hossain, Y. Himuro, et al.; Simulation of Molten Metal Penetration and Freezing Behavior in a Seven-Pin Bundle Experiment", Journal of Nuclear Science and Technology, Vol. 46, No. 8, pp. 799-808 (2009).

8) M. A. Malek Soner, Y. Hasegawa, et al.; Experimental Study on Penetration and Freezing Behavior of Solid-liquid Multiphase Flow in Pin Bundle Geometry", Proceedings of the 7th Korea-Japan Symposium on Nuclear Thermal Hydraulics and Safety, November 14-17, Chuncheon, Korea (2010).

9) S. Kondo, K. Konishi, et al.; Experimental Study on Simulated Molten Jet-Coolant Interactions", Nuclear Engineering and Design 155, pp. 73–84 (1995).

10) W. Liu, G. X. Wang, et al.; Thermal Analysis and Measurements for a Molten Metal Drop Impacting on a Substrate: Cooling, Solidification and Heat Transfer Coefficient", International Journal of Heat and Mass Transfer 38 (8), pp. 1387–1395 (1995).

11) H. K. Fauske, K. Koyama, et al.; Assessment of FBR Core Disruptive Accident (CDA): The Role and Application of General Behavior Principles (GBPs), Journal of Nuclear Science and Technology 39 (6), pp. 615–627 (2002).

12) K. Morita, Y. Tobita, et al.; SIMMER-III Heat-and Mass-Transfer Model – Model and Method Description" JNC TN9400 2001-074, Japan Nuclear Cycle Development Institute (2001).

13) W. B. Russel, Effects of Interaction between Particles and Rheology of Dispersions," Theory of Dispersed Multiphase Flow, R. E. Meyer, Academic Press, New York (1983).

14) Y. Tobita, Momentum Exchange Function Model in SIMMER-III (Research Document), Japan Nuclear Cycle Development Institute, to be published.

15) W. R. Bohl, L. B. Luck, et al.; SIMMER-II: A Computer Program for LMFBR Disrupted Core Analysis", Los Alamos National Laboratory, LA-11415-MS (1990).

16) J. J. Sienicki, B. W. Spencer, et al.; Freezing Controlled Penetration of Molten Metals Flowing Through Stainless Steel Tubes," ANS Proc. of 1985 National Heat Transfer Conference, Denver, USA, August 4-7,   pp. 245-254 (1985).

17) D. G. Thomas, Transport Characteristics of Suspension': VIII. A Note on the Viscosity of Newtonian Suspensions of Uniform Spherical Particles" Journal of Colloid Science, 20, pp. 267-277 (1965).